Rigid Body Modeling and Dynamic Flight Control of a Tethered Kite

Enso Ndreko, Monika Pasquali, Tudor-Bogdan Airimitoaie, Christophe Farges, Patrick Lanusse

▶ **To cite this version:**

Enso Ndreko, Monika Pasquali, Tudor-Bogdan Airimitoaie, Christophe Farges, Patrick Lanusse. Rigid Body Modeling and Dynamic Flight Control of a Tethered Kite. 12th International Conference on Control, Mechatronics and Automation (ICCMA), Nov 2024, London, United Kingdom. pp.415-420, ⟨10.1109/ICCMA63715.2024.10843908⟩. ⟨hal-04930312⟩

HAL Id: hal-04930312

https://hal.science/hal-04930312v1

Submitted on 5 Feb 2025

HAL is a multi-disciplinary open access archive for the deposit and dissemination of scientific research documents, whether they are published or not. The documents may come from teaching and research institutions in France or abroad, or from public or private research centers.

L'archive ouverte pluridisciplinaire **HAL**, est destinée au dépôt et à la diffusion de documents scientifiques de niveau recherche, publiés ou non, émanant des établissements d'enseignement et de recherche français ou étrangers, des laboratoires publics ou privés.

Distributed under a Creative Commons CC BY-NC-SA 4.0 - Attribution - Non-commercial use - ShareAlike - International License

Rigid Body Modeling and Dynamic Flight Control of a Tethered Kite

Enso Ndreko
Univ. Bordeaux, CNRS, Bordeaux INP, IMS, 33400 Talence, France
enso.ndreko@ims-bordeaux.fr

Monika Pasquali
Univ. Bordeaux, CNRS, Bordeaux INP, IMS, 33400 Talence, France
monika.pasquali@ims-bordeaux.fr

Tudor-Bogdan AIRIMITOAIE
Univ. Bordeaux, CNRS, Bordeaux INP, IMS, 33400 Talence, France
tudor-bogdan.airimitoaie@ims-bordeaux.fr

Christophe FARGES
Univ. Bordeaux, CNRS, Bordeaux INP, IMS, 33400 Talence, France
christophe.farges@ims-bordeaux.fr

Patrick LANUSSE
Univ. Bordeaux, CNRS, Bordeaux INP, IMS, 33400 Talence, France
patrick.lanusse@ims-bordeaux.fr

***Abstract*—Concerns about CO_2 emissions and rising oil costs are fueling the search for alternative energy sources, including wind power for maritime transportation. The *Beyond the Sea* enterprise led by Yves Parlier, seeks the usage of tethered kites as a sustainable propulsion solution for vessels.**

This study explores a Lagrangian rigid body model that closely replicates a real-life experimental setup on the beach, incorporating parameters with physical significance and accounting for inertia effects. Keeping the kite in the desired part of the flying window is managed by guiding it along figure-eight trajectories, with adjustable parameters for position, size, and orientation.

A trajectory-following control strategy is employed to ensure alignment to the desired path. The model's accuracy and the effectiveness of the control methodology are qualitatively validated through simulations and animations of the kite's takeoff and dynamic flight across various trajectories.

***Index Terms*—AWE, Kite modeling, Lagrangian system, Kite control, Dynamic flight, Kite animation**

I. Introduction

The pressing need to reduce CO_2 emissions and the increasing oil prices are significantly affecting all transportation sectors, especially the maritime industry. Consequently, there is a rising interest in discovering alternative methods to diminish environmental impact and lower fuel consumption. A promising recent solution is the integration of Airborne Wind Energy (AWE) systems. These systems use tethered kites, similar to those used in kite surfing and others, to convert the traction power of airfoils into electrical energy [1], [2] or into propulsion energy for vessels [3], [4].

Moreover, since AWE systems operate at higher altitudes, they can access a variety of wind resources. This capability, combined with their low mass, results in a high mass-performance ratio, enhancing the overall efficiency and reliability of the installation. These attributes make AWE systems particularly well-suited for the marine environment.

Previous research on automated kite control has largely focused on point mass models [5]–[11]. While these models have been validated and used for initial control efforts by *Beyond the sea* [9], they treat the kite as a singular point in the flight window. This simplification means they do not consider the kite's rotational dynamics around its center of mass and their inertial effects, resulting in a lack of accuracy necessary for more advanced analysis and control. In fact, to account for this, they often rely on an empirical expression for yaw speed.

To overcome the limitations of point mass models, more advanced approaches have been developed. One method uses multiple interconnected point masses to better represent the kite's structure and dynamics [12]. Another approach models the kite as a rigid body [13]–[19], striking an effective balance between precision and computational efficiency. Furthermore, flexibility effects have been incorporated into kite flight simulations through a multibody-system model reduction process [20], enhancing the realism and fidelity of the results.

Single-kite systems, like the one outlined in this paper, work in periodic cycles to maximize the traction force by guiding the kite through rapid crosswind maneuvers. By following figure-eight patterns, these systems boost energy capture since they are flying in cross-wind, prevent tether entanglement, and maintain a continuous, efficient flight path.

In this study, Section II replicates a four-line tethered kite experimental setup in the beach used by *Beyond the Sea* enterprise. This is achieved using a rigid body model specifically adapted for our system, which take into account inertial behaviors and where all the parameters have clear physical meanings. Section III focuses on the trajectory-following algorithm, necessary for the kite to adhere to the desired path, and outlines the control strategy. In Section IV, we implement the close-loop system using the model and trajectory-following strategy to animate and simulate the kite's flight dynamics from takeoff to sustained dynamic flight. Finally, Section V provides conclusions and perspectives of the work.

II. Kite Model Description

In this section, we present our kite model, which treats the kite as a rigid structure, ignoring its flexibility and elasticity.

This project was funded by the French state as part of France 2030.

This approach draws inspiration from works such as [14], [17], [19], which use Lagrangian mechanics to model various kite systems, including a surf-kite system controlled by a kite-surfer. In our case, the model corresponds to an experimental setup on the shore, with control implemented via DC motors.

Fig. 1 illustrates our system with a four-line LEI (Leading Edge Inflatable) kite. No air intakes or stabilizers are included. The two front lines (OF_R and OF_L) converge at a common point O. These lines are modeled as massless, inelastic, and non-flexible, which is a reasonable approximation under high traction. Given these assumptions and the kite's rigidity, the triangle F_ROF_L maintains its shape anytime and can be represented by a single parameter L, denoting its height.

On the other side, the back lines, E_RB_R and E_LB_L are considered elastic, but yet massless and not flexible. Because of this, besides their original lengths L_t, the elasticity effect is taken into account by e_R and e_L.

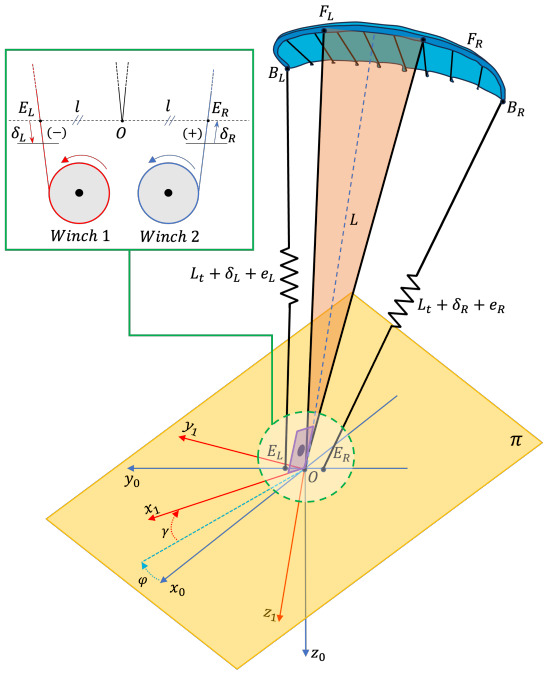

Fig. 1: Kite system representation and R_0/R_1 reference frames.

The two back lines serve also as control lines using two winches rotated by DC motors, as shown in Fig. 1. In this strategy, the control input is defined as $\delta = \delta_R - \delta_L$, where $|\delta_L| = |\delta_R| = \left|\frac{\delta}{2}\right|$.

A. Reference Systems

Defining the necessary reference systems is crucial. Our primary reference is the ground frame R_0, with its origin at point O. In this frame, x_0-axis points away from the flight window towards the operator, z_0-axis aligns with the direction of gravitational force, and y_0-axis is oriented to complete a right-handed coordinate system, forming the plane π with x_0-axis.

R_1 frame gives us a plane perpendicular to triangle F_ROF_L by rotating first around z_0 and then around y_1:

$$\mathbf{R_{1-0}} = \mathbf{R}(\overrightarrow{j_1}, \gamma)\mathbf{R}(\overrightarrow{k_0}, \varphi) \tag{1}$$

$$= \begin{bmatrix} c(\gamma) & 0 & -s(\gamma) \\ 0 & 1 & 0 \\ s(\gamma) & 0 & c(\gamma) \end{bmatrix} \begin{bmatrix} c(\varphi) & -s(\gamma) & 0 \\ s(\varphi) & c(\varphi) & 0 \\ 0 & 0 & 0 \end{bmatrix}. \tag{2}$$

Fig. 1 shows these two reference frames.

Besides R_0 and R_1, R_2 frame takes into account the rotation of the triangle F_ROF_L around x_1-axis, as shown in Fig. 2a:

$$\mathbf{R_{2-1}} = \mathbf{R}(\overrightarrow{i_1}, \eta) \tag{3}$$

$$= \begin{bmatrix} 1 & 0 & 0 \\ 0 & c(\eta) & s(\eta) \\ 0 & -s(\eta) & c(\eta) \end{bmatrix}. \tag{4}$$

The body reference frame is centered at the kite's center of gravity G, where the x_G-axis is aligned with the kite's main cord to indicate its orientation. R_G is defined by rotating around y_2 as illustrated in Fig. 2b:

$$\mathbf{R_{G-2}} = \mathbf{R}(\overrightarrow{j_2}, \vartheta) \tag{5}$$

$$= \begin{bmatrix} c(\vartheta) & 0 & -s(\vartheta) \\ 0 & 1 & 0 \\ s(\vartheta) & 0 & c(\vartheta) \end{bmatrix}. \tag{6}$$

On R_G, we can define the positions $F_{L/R}(x_F, \pm y_F, z_F)$ and $B_{L/R}(x_B, \pm y_B, z_B)$.

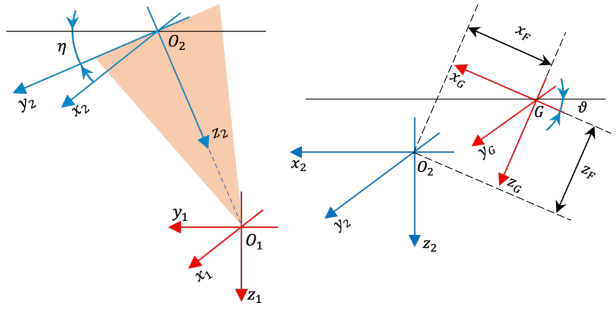

(a) R_2 Reference frame. (b) R_G Reference frame.

Fig. 2: Graphical representation of R_2 and R_G frames.

With these definitions, we establish a four DOF system with the generalized coordinate vector:

$$\mathbf{q} = [\varphi \quad \gamma \quad \eta \quad \vartheta]^T. \tag{7}$$

B. Lagrangian Formalism

The Lagrangian mechanics is based on the solutions of Euler-Lagrangian equation [21], [22], which is expressed as:

$$\frac{d}{dt}\left(\frac{\partial L}{\partial \dot{q}_n}\right) - \frac{\partial L}{\partial q_n} = Q_n, \tag{8}$$

where, $L = E_K - E_P$ is the Lagrangian of the system, q_n is the n^{th} generalized coordinate, $\dot{q}_n$ is the n^{th} generalized velocity, and Q_n the n^{th} generalized force.

C. Kinetic and Potential Energy

The kite's center of mass, expressed in the R_0 frame, is:

$$\overrightarrow{r}_G^0 = \mathbf{R_{2-0}^T} \begin{bmatrix} 0 \\ 0 \\ -L \end{bmatrix} + \mathbf{R_{G-0}^T} \begin{bmatrix} -x_F \\ 0 \\ -z_F \end{bmatrix}, \tag{9}$$

where, $\mathbf{R_{2-0}} = \mathbf{R_{2-1}R_{1-0}}$ and $\mathbf{R_{G-0}} = \mathbf{R_{G-2}R_{2-1}R_{1-0}}$. Thus, we can derive the gravitational potential energy as:

$$E_P = -m_k g H \tag{10}$$

$$= -m_k g \overrightarrow{r}_G^0 \begin{bmatrix} 0 \\ 0 \\ 1 \end{bmatrix}, \tag{11}$$

where, m_k is the mass of the kite and g the gravitational acceleration.

Also, since $\dot{\vec{r}}^m = \dot{\mathbf{R}}_{\mathbf{m-n}}\vec{r}^n + \mathbf{R_{m-n}}\dot{\vec{r}}^n = \vec{\omega} \times [\mathbf{R_{m-n}}\vec{r}^n] + \mathbf{R_{m-n}}\dot{\vec{r}}^n$, with m and n reference frames, we can express the kite's linear velocity in the body frame R_G as:

$$\overrightarrow{v}_G^G = \mathbf{R_{G-2}} \left[\overrightarrow{\omega}_{2-0} \times \begin{bmatrix} 0 \\ 0 \\ -L \end{bmatrix} \right] + \overrightarrow{\omega}_{G-0} \times \begin{bmatrix} -x_F \\ 0 \\ -z_F \end{bmatrix}, \tag{12}$$

where, the angular velocities $\vec{\omega}_{2-0} = \dot{\eta}\vec{i}_2 + \mathbf{R_{2-0}}\dot{\varphi}\vec{k}_0 + \mathbf{R_{2-1}}\dot{\gamma}\vec{j}_1$ and $\vec{\omega}_{G-0} = \dot{\vartheta}_G + \mathbf{R_{G-2}}\dot{\eta}\vec{i}_2 + \mathbf{R_{G-0}}\dot{\varphi}\vec{k}_0 + \mathbf{R_{G-1}}\dot{\gamma}\vec{j}_1$. Furthermore, by algebraic transformations, we can express $\vec{v}_G^G$ and $\vec{\omega}_{G-0}$ as:

$$\overrightarrow{v}_G^G = \mathbf{\Psi}\dot{\mathbf{q}}, \quad \mathbf{\Psi} \in \mathbb{R}^{3\times 4}, \tag{13}$$

$$\overrightarrow{\omega}_{G-0} = \mathbf{\Omega}\dot{\mathbf{q}}, \quad \mathbf{\Omega} \in \mathbb{R}^{3\times 4}. \tag{14}$$

These expressions allow us to calculate the kinetic energy of our system, which comes from both the translational component and the rotational one as $E_k = \frac{1}{2}m_k v^2 + \frac{1}{2}I_G\omega^2$ in the matrix form:

$$E_K = \frac{1}{2}\dot{\mathbf{q}}^T \underbrace{\left[\mathbf{\Psi}^T(m_k\mathbf{I})\mathbf{\Psi} + \mathbf{\Omega}^T\mathbf{I_G}\mathbf{\Omega}\right]}_{\mathbf{M}} \dot{\mathbf{q}}, \tag{15}$$

where, $\mathbf{I} \in \mathbb{R}^{3\times 3}$ is an identity matrix and $\mathbf{I_G} \in \mathbb{R}^{3\times 3}$ the inertia tensor at the center of mass G. The component $\mathbf{M} \in \mathbb{R}^{4\times 4}$ represents the generalized inertia matrix and, as shown from the equation, is composed from translational inertia contributions $\mathbf{\Psi}^T(m_k\mathbf{I})\mathbf{\Psi}$ and the rotational inertia contributions $\mathbf{\Omega}^T\mathbf{I_G}\mathbf{\Omega}$.

D. Generalized Forces

In this section, we introduce the concept of generalized forces within our system. We begin by considering the non-conservative forces and moments, such as aerodynamic ones:

$$\overrightarrow{F}_A^G = \bar{q} \begin{bmatrix} C_D \\ C_S \\ C_L \end{bmatrix} = \bar{q} \begin{bmatrix} C_{x0} + C_{x\alpha}\alpha \\ C_{y\beta}\beta \\ C_{z0} + C_{z\alpha}\alpha \end{bmatrix}, \tag{16}$$

$$\overrightarrow{M}_A^G = \bar{q} \begin{bmatrix} bC_l \\ cC_m \\ bC_n \end{bmatrix} = \bar{q} \begin{bmatrix} b(C_{l\beta}\beta + C_{lp}\frac{b\omega_{G-0,\vec{i}}}{2v_T}) \\ c(C_{m0} + C_{m\alpha} + C_{mq}\frac{c\omega_{G-0,\vec{j}}}{v_T}) \\ b(C_{n\beta}\beta + C_{nr}\frac{b\omega_{G-0,\vec{k}}}{2v_T} + C_{nt}t) \end{bmatrix}, \tag{17}$$

with $\bar{q} = \frac{1}{2}\rho S \left\| \overrightarrow{v}_a \right\|^2$ defining the dynamic pressure, ρ the air density, S the kite's surface, and $\overrightarrow{v}_a^G = \overrightarrow{v}_G^G - \overrightarrow{v}_w^G$ the apparent velocity described as the difference between kite's velocity and wind velocity in the body frame. The angle of attack and the side-slip angle correspond to $\alpha = \arctan \frac{v_{a,\vec{k}}^G}{v_{a,\vec{i}}^G}$ and $\beta = \arcsin \frac{v_{a,\vec{j}}^G}{\|\overrightarrow{v}_a^G\|}$.

In (17) the parameters b and c stand for the span and for the cord of the kite, while v_T is a reference velocity and t reflects the aerodynamic yaw moment resulting from the kite's deformation due to the differing tensions at the back lines. Air resistance is accounted for, mainly, in the drag force $F_A^G\vec{i}$. Given the sensitivity of aerodynamic models and their coefficients, we have employed here the representations found in [17], [23].

Besides the aerodynamic forces, the conservative traction forces applied by the elastic back lines, should be considered too. To derive this, we define first:

$$\overrightarrow{E_{R/L}^G B_{R/L}^G} = \mathbf{R_{G-0}} \left[\begin{bmatrix} 0 \\ \pm l \\ 0 \end{bmatrix} + \overrightarrow{r}_G^0 + \begin{bmatrix} x_B \\ \mp y_B \\ z_B \end{bmatrix} \right], \tag{18}$$

and noting $L_{R/L} = \left\| \overrightarrow{E_{R/L}^G B_{R/L}^G} \right\|$.

Due to the elasticity of the back lines, we first define the Cauchy stress using Hooke's Law as follows:

$$\sigma_{R/L} = -E\frac{L_{R/L} - (L_t \pm \delta/2)}{L_t \pm \delta/2}, \tag{19}$$

with E the Young modulus. Knowing that the $F = \sigma S_t$, with S_t being the line cross-section area, we find the tensions $\overrightarrow{T}_R$ and $\overrightarrow{T}_L$ as:

$$\overrightarrow{T}_{R/L}^G = -ES_t\frac{L_{R/L} - (L_t \pm \delta/2)}{L_t \pm \delta/2} \underbrace{\frac{\overrightarrow{E_{R/L}^G B_{R/L}^G}}{L_{R/L}}}_{\overrightarrow{u}_{R/L}}, \tag{20}$$

where, $\overrightarrow{u}_{R/L}$ is the unit vector showing the direction of the tension force applied along the right and left line. On the other hand, the moments created by these forces are the following:

$$\overrightarrow{M}_{R/L}^G = \begin{bmatrix} x_B \\ \mp y_B \\ z_B \end{bmatrix} \times \overrightarrow{T}_{R/L}^G. \tag{21}$$

Therefore, the resultants of these forces and moments applied on the kite are $\overrightarrow{F}_R = \overrightarrow{F}_A^G + \overrightarrow{T}_R^G + \overrightarrow{T}_L^G$ and $\overrightarrow{M}_R = \overrightarrow{M}_A^G + \overrightarrow{M}_R^G + \overrightarrow{M}_L^G$, respectively. This gives us the final expression of the generalized forces:

$$Q_n = F_{R,p}\frac{\partial v_{G,p}^G}{\partial \dot{q}_n} + M_{R,p}\frac{\partial \omega_{G-0,p}}{\partial \dot{q}_n}, \quad n = 1,2,3,4, \tag{22}$$

with n being the index of the generalized coordinate.

E. Lagrangian Model

Finally, by having all the components of the Euler-Lagrangian equation (8), we end up with four nonlinear differential equations:

$$M_{nm}\ddot{q}_m + \frac{\partial M_{nm}}{\partial q_p}\dot{q}_p\dot{q}_m - \frac{1}{2}\frac{\partial M_{mp}}{\partial q_n}\dot{q}_m\dot{q}_p + \frac{\partial E_P}{\partial q_n} = Q_n. \tag{23}$$

Equations (22) and (23) are expressed in the Einstein's tensor notation, and describe the behavior of our kite system.

III. Kite Control Strategy

A key aspect of this work is developing a control scheme to guide the kite along a specified path T_{des}. As discussed in Section I, a Bernoulli lemniscate is ideal for preventing line tangling and maximizing traction. This trajectory is defined by the following parametric equations with the parameter s:

$$\begin{cases} x_T = a\frac{\sin(s)}{1+\cos^2(s)}, \\ y_T = a\frac{\cos(s)\sin(s)}{1+\cos^2(s)}, \end{cases} \tag{24}$$

with $s \in [0, 2\pi]$, which shows that the trajectory is independent of time, implying that following the path is a spatial rather than temporal process. Consequently, the trajectory is spatially discretized into a sequence of points P.

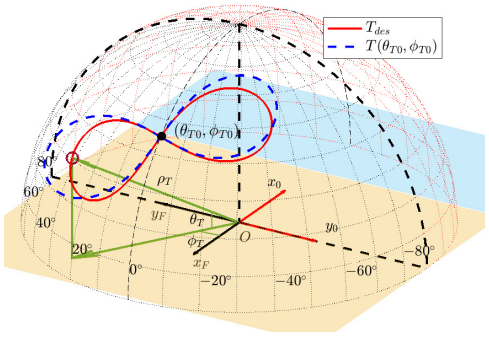

Fig. 3: Reference frame R_F, the spherical coordinates and $T(\theta_{T0}, \phi_{T0})$, Bernoulli's lemniscate tangent to the point (θ_{T0}, ϕ_{T0}) rotated with an angle Θ_s, together with T_{des}, its projection to the flight window, in a beach environment.

For simplicity, since the kite always flies towards the negative x_0-axis, we introduce a new reference system R_F by rotating R_0 with $\mathbf{R_{F-0}} = \mathbf{R}(\overrightarrow{k_0}, \pi)$.

It is useful to express the desired trajectory $T_{\text{des}}(\rho_T, \theta_T, \phi_T)$ and the kite's position $\overrightarrow{r}^F_G(\rho_G, \theta_G, \phi_G)$ in spherical coordinates, as shown in Fig. 3. Due to the elasticity of the back lines, ρ_G varies slightly, making it crucial for defining $\overrightarrow{r}^F_G$. In contrast, T_{des} has a constant ρ_T, simplifying the trajectory to $T_{\text{des}}(\theta_T, \phi_T)$.

To fully define the trajectory, the parameters (θ_{T0}, ϕ_{T0}) for the initial position, Θ_s for the planar rotation around (θ_{T0}, ϕ_{T0}), and a for the arc length are necessary. Once the lemniscate is parameterized, its origin is positioned at (θ_{T0}, ϕ_{T0}) in a plane tangent to the flight window and then mapped into the quarter sphere (see Fig. 3).

A. Trajectory-following algorithm

The main goal is for the kite to reach and precisely follow the designated trajectory [24]–[26]. To achieve this, Algorithm 1 minimizes the distance to the desired trajectory and aligns the kite's velocity with the trajectory's tangent.

Algorithm 1 Trajectory-Following

1: Set initial point P_i as P_{opt}.
2: Define reference frame R_P at P_{i+1}.
3: **while** $t = t_0$ to t_n **do**
4: **if** $x^P_G(t) > 0$ **then**
5: Update P_{opt} to P_{i+1}.
6: Define new reference frame R_P at P_{i+2}.
7: $i = i + 1$.
8: **end if**
9: Calculate $\chi_{cmd} = \chi_c(i) + \Delta\chi_{cmd}(t)$, where $\chi_c \approx \widehat{\vec{j}_k\vec{i}_P}$ and $\Delta\chi_{cmd}(d) = \arctan\frac{d}{d_0}$ with $d(t) \approx y^P_G(t)$.
10: Calculate $\chi(t) = \widehat{\vec{j}_k\vec{V}^k_G}(t)$.
11: Calculate $\epsilon_\chi = \chi - \chi_{cmd}$.
12: **end while**

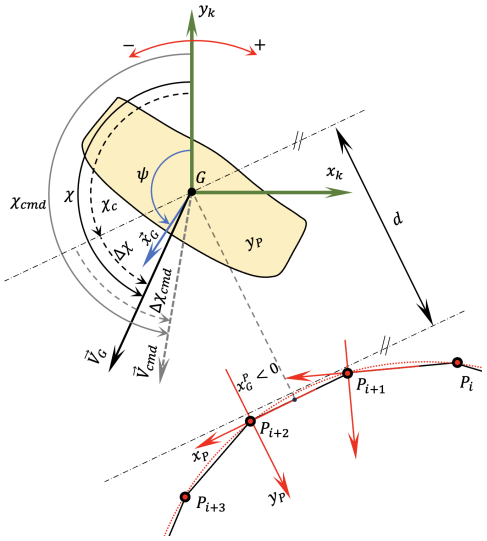

Fig. 4: Trajectory-Following scenario, with the corresponding parameters and reference systems.

At each time step t, the algorithm determines which point of T_{des} the kite should follow as it is flying, by determining the kite's position at the current provisory R_P, as shown in Fig. 4. R_P is defined with the x_P-axis directed from the P_{opt} (ex. P_{i+1}) to the next P point (P_{i+2}), z_P directed from the origin O to the next P point and y_P forms a right hand reference system. As long as the kite's coordinate $x^P_G < 0$, the R_P stays in the same point, until when $x^P_G > 0$, then it moves to the new one.

The desired velocity angle χ_{cmd} must be computed and then compared to the current angle χ, as explained in Algorithm 1.

To understand all the angles used in here, another reference system R_k is introduced. Its y_k-axis is tangent to the flight window and is laid along the meridian passing threw point G, directed towards the zenith. z_k is pointing towards the O origin of R_F and x_k forms a right hand reference system with the two other axes (see Fig. 4).

The angle χ_{cmd} is composed of χ_c and $\Delta\chi_{\text{des}}(d)$ [26], shown again in Fig. 4. The first term is the angle between j_k and the tangent of T_{des}, which makes the kite has the same alignment, but not necessarily the same trajectory. The second one, $\Delta\chi_{cmd}(d) = \arctan\frac{d}{d_0}$, is needed to help the kite move closer to the desired trajectory. When the kite is far from T_{des} ($d \gg d_0$), $\Delta\chi_{\text{des}} \approx 90°$, directing the kite straight towards the trajectory. If $d \ll d_0$, $\Delta\chi_{\text{des}} \approx 0°$, the kite is primarily following the trajectory. This parameter d_0 can be set as a constant value or adjusted dynamically based on the kite's speed.

B. Control Strategy

The close-loop scheme is the final step in controlling the kite to follow the desired trajectory T_{des}. Fig. 5 shows the block diagram of this system, which includes the controller, the rigid body kite model from Section II, and the trajectory-following blocks that calculate χ and χ_{cmd}. The difference between χ and χ_{cmd}, denoted as ϵ_χ, is tended to be 0 by the reference signal.

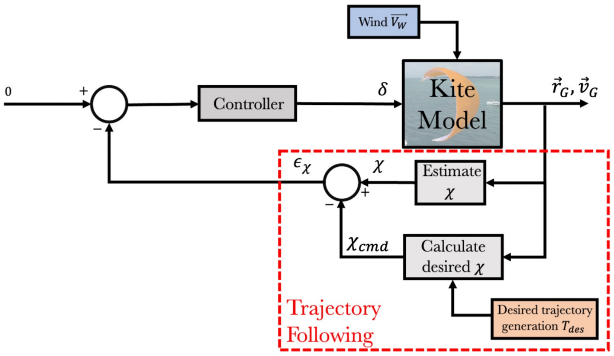

Fig. 5: Close-loop control.

IV. Close-loop simulation

In this section, simulations are conducted using MATLAB/Simulink, implementing the control strategy illustrated in Fig. 5. For our simulation purposes, a proportional controller proved effective by trials. The physical parameters of the kite and the aerodynamic coefficients are sourced from [17], with a $V_W = 7m/s^2$ in the x_F-axis direction, $L = 24.55m$, $L_t = 23.19m$ and $l = \mid E_{L/R}O \mid = 0.28m$.

Fig. 6a presents the results of a kite animation following a desired trajectory T_{des}, in the center of the flight window, with $a = 10$, $(\theta_{T0}, \phi_{T0}) = (45°, 0°)$ and $\Theta_s = 0°$. Initially at rest, the kite starts from $\mathbf{q_0} = [0 \quad 80° \quad 0 \quad 0]^T$, takes off, and enters dynamic flight. A $d_0 = 1.5m$ is chosen by trials for $\Delta\chi_{cmd}$.

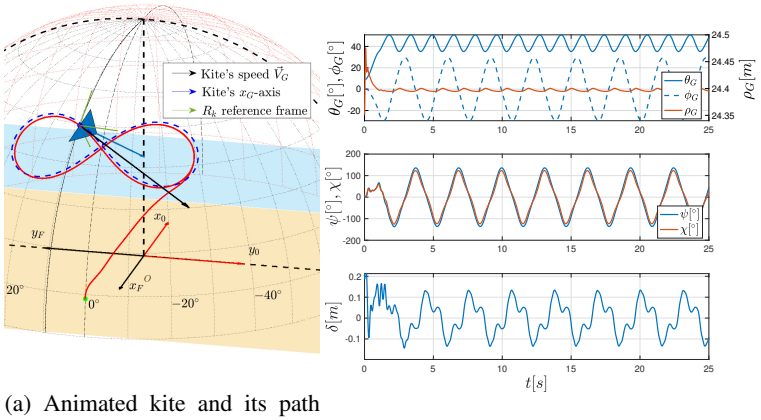

(a) Animated kite and its path (red), following T_{des} (blue).

(b) Simulation results.

Fig. 6: Takeoff and dynamical flight simulation following the T_{des}.

In Fig. 6b, we observe the spherical coordinates of the kite (G origin), the yaw angle ψ, the speed angle χ, and the symmetric control command δ. Notably, ψ and χ are very close, indicating that the kite is well-oriented along its trajectory. A behavior consistent with real-life experiments and that gives us qualitative validation of our model.

Worth emphasizing that since a rigid body model is used, the takeoff dynamics ($t = [0, 1.5]s$) are physically accounted for by the model, including the ψ movement.

Another interesting simulation occurs when the kite transitions from one figure-eight pattern to another during the flight. In Fig. 7, we illustrate multiple trajectories where θ_{T0} varies from 20° to 60° in increments of 10°. In this scenario, we

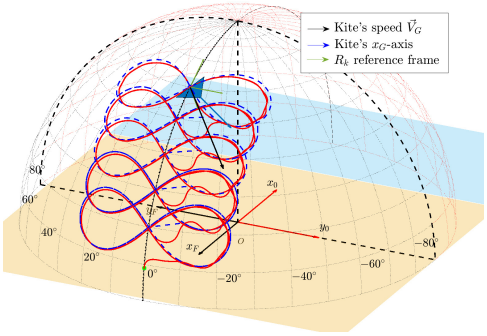

Fig. 7: Animated flying kite changing T_{des} in flight.

observe that when the kite changes its trajectory, there is a transient phase before it stabilizes and resumes following T_{des}.

Animations of the kite during dynamic flight were also produced with various trajectories and different takeoff positions to demonstrate the flexibility of the methodology. In Fig. 8, the green kite follows a desired trajectory T_{des} with $a = 10$, $(\theta_{T0}, \phi_{T0}) = (27°, 0°)$, and $\Theta_s = 90°$. The red kite follows a T_{des} with $a = 13$, $(\theta_{T0}, \phi_{T0}) = (40°, -45°)$, and $\Theta_s = -60°$. The blue kite's T_{des} has $a = 10$, $(\theta_{T0}, \phi_{T0}) = (40°, 30°)$, and $\Theta_s = 30°$. It is worth mentioning that studies can be conducted to determine the optimal trajectory in the flight window for

specific wind conditions [27], which can then be implemented into our control scheme.

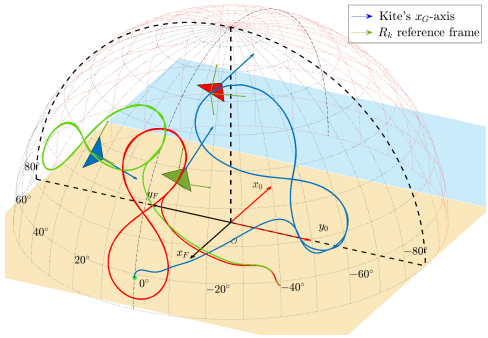

Fig. 8: Animated flying kites exploring different trajectories.

V. Conclusions

In this work, we initially presented a rigid body Lagrangian model for our four-line LEI kite experimental setup on the beach, controlled by two DC motors. To simplify the model and achieve a balance between complexity and accuracy from a control system perspective, we introduced constraints such as the rigidity of the kite and of the two front lines. As a result, we developed a mathematical model where all parameters have physical significance, avoiding the use of empirical expressions to describe the kite's behavior. However, future work will involve adjusting this model to align with real experimental setup parameters. This task also includes selecting reliable aerodynamic force and moment models and accurately estimating their coefficients.

We required the kite to follow a Bernoulli's lemniscate trajectory projected into the flight window. To achieve this, a trajectory-following algorithm was implemented in a close-loop system. This algorithm aims to minimize the distance between the kite's position and the desired trajectory while simultaneously aligning the kite with it. A proportional controller, sufficient for simulations and demonstrating methodology, was integrated into the closed-loop system. Finally, the close-loop system (excluding the actuators) was completed, and enabling simulations. A more robust and sufficient controller will be developed at a later stage.

The standard scenario, featuring a horizontal lemniscate as the trajectory positioned at the center of the flight window, was simulated from takeoff through dynamic flight. In this case, the yaw and speed angles were compared and found to be closely aligned, consistent with experimental observations. Additionally, simulations were performed with a kite changing its trajectory in flight and kites following vertical, inclined, and off-center trajectories. Although these paths are not commonly used, they demonstrate the feasibility of alternative trajectories and provide opportunities for traction force studies.

References

[1] Lansdorp, B., Ruiterkamp, R. & Ockels, W. Towards flight testing of remotely controlled surfkites for wind energy generation. *AIAA Atmospheric Flight Mechanics Conference And Exhibit*. pp. 6643 (2007)

[2] De Wachter, A. Power from the skies: Laddermill takes airborne wind energy to new heights. *Leonardo Times, 14 (Dec) 2010*. (2010)

[3] Wellicome, J. Some comments on the relative merits of various wind propulsion devices. *Journal Of Wind Engineering And Industrial Aerodynamics*. **20**, 111-142 (1985)

[4] Leloup, R., Roncin, K., Behrel, M., Bles, G., Leroux, J., Jochum, C. & Parlier, Y. A continuous and analytical modeling for kites as auxiliary propulsion devoted to merchant ships, including fuel saving estimation. *Renewable Energy*. **86** pp. 483-496 (2016)

[5] Loyd, M. Crosswind kite power (for large-scale wind power production). *Journal Of Energy*. **4**, 106-111 (1980)

[6] Ahmed, M., Hably, A. & Bacha, S. Kite generator system modeling and grid integration. *IEEE Transactions On Sustainable Energy*. **4**, 968-976 (2013)

[7] Erhard, M. & Strauch, H. Control of towing kites for seagoing vessels. *IEEE Transactions On Control Systems Technology*. **21**, 1629-1640 (2012)

[8] Canale, M., Fagiano, L. & Milanese, M. High altitude wind energy generation using controlled power kites. *IEEE Transactions On Control Systems Technology*. **18**, 279-293 (2009)

[9] Griffon, P. Modelling and control of a tethered kite in dynamic flight. (2017)

[10] Wood, T., Hesse, H., Polzin, M., Ahbe, E. & Smith, R. Modeling, identification, estimation and adaptation for the control of power-generating kites. *IFAC-PapersOnLine*. **51**, 981-989 (2018)

[11] Dief, T., Fechner, U., Schmehl, R., Yoshida, S., Ismaiel, A. & Halawa, A. System identification, fuzzy control and simulation of a kite power system with fixed tether length. *Wind Energy Science*. **3**, 275-291 (2018)

[12] Fechner, U., Vlugt, R., Schreuder, E. & Schmehl, R. Dynamic model of a pumping kite power system. *Renewable Energy*. **83** pp. 705-716 (2015)

[13] Sánchez, G. Dynamics and control of single-line kites. *The Aeronautical Journal*. **110**, 615-621 (2006)

[14] Sánchez-Arriaga, G., Pastor-Rodriguez, A., Sanjurjo-Rivo, M. & Schmehl, R. A lagrangian flight simulator for airborne wind energy systems. *Applied Mathematical Modelling*. **69** pp. 665-684 (2019)

[15] Williams, P., Lansdorp, B. & Ockesl, W. Optimal crosswind towing and power generation with tethered kites. *Journal Of Guidance, Control, And Dynamics*. **31**, 81-93 (2008)

[16] Gros, S. & Diehl, M. Modeling of airborne wind energy systems in natural coordinates. *Airborne Wind Energy*. pp. 181-203 (2013)

[17] Sanchez-Arriaga, G., Pastor-Rodrıiguez, A., Borobia-Moreno, R. & Schmehl, R. A constraint-free flight simulator package for airborne wind energy systems. *Journal Of Physics: Conference Series*. **1037**, 062018 (2018)

[18] Pastor-Rodrıiguez, A., Sanchez-Arriaga, G. & Sanjurjo-Rivo, M. Modeling and stability analysis of tethered kites at high altitudes. *Journal Of Guidance, Control, And Dynamics*. **40**, 1892-1901 (2017)

[19] Sánchez-Arriaga, G., Garcıia-Villalba, M. & Schmehl, R. Modeling and dynamics of a two-line kite. *Applied Mathematical Modelling*. **47** pp. 473-486 (2017)

[20] De Groot, S., Breukels, J., Schmehl, R. & Ockels, W. Modelling kite flight dynamics using a multibody reduction approach. *Journal Of Guidance, Control, And Dynamics*. **34**, 1671-1682 (2011)

[21] Bona, B. Dynamic Modelling of Mechatronic Systems. (2013), https://api.semanticscholar.org/CorpusID:59625135

[22] Landau, Lev Davidovich, and Lifshitz, Evgenii Mikhailovich. *Mechanics*. Volume 1, 1960.

[23] Stevens, B. L., Lewis, F. L., & Johnson, E. N. (2015). *Aircraft control and simulation: dynamics, controls design, and autonomous systems*. John Wiley & Sons.

[24] Cadalen, B., Lanusse, P., Sabatier, J., Griffon, F. & Parlier, Y. Robust control of a tethered kite for ship propulsion. *2018 European Control Conference (ECC)*. pp. 3065-3070 (2018)

[25] Cadalen, B., Sabatier, J., Lanusse, P., Griffon, F. & Parlier, Y. A Control Solution for a Tethered Kite Trajectory Tracking With Application to Ship Propulsion. *Journal Of Dynamic Systems, Measurement, And Control*. **142**, 121002 (2020)

[26] Jehle, C. Automatic flight control of tethered kites for power generation. (2012)

[27] Monika Pasquali, Enso Ndreko, Tudor-Bogdan Airimitoaie, Christophe Farges, Patrick Lanusse. "Optimal flight trajectories of a tethered kite for ship propulsion under variable wind conditions". 12th ICCMA 2024 (In press)